PHILOSOPHICAL
TRANSACTIONS A

royalsocietypublishing.org/journal/rsta

Research

Cite this article: Crowley CJ, Pughe-Sanford JL, Toler W, Grigoriev RO, Schatz MF. 2023 Observing a dynamical skeleton of turbulence in Taylor–Couette flow experiments. *Phil. Trans. R. Soc. A* **381**: 20220137. https://doi.org/10.1098/rsta.2022.0137

Received: 2 August 2022
Accepted: 31 October 2022

One contribution of 16 to a theme issue 'Taylor–Couette and related flows on the centennial of Taylor's seminal *Philosophical Transactions* paper (part 1)'.

Subject Areas:
fluid mechanics, chaos theory

Keywords:
coherent structures, periodic orbits, shadowing

Author for correspondence:
M. F. Schatz
e-mail: michael.schatz@physics.gatech.edu

Observing a dynamical skeleton of turbulence in Taylor–Couette flow experiments

C. J. Crowley[†], J. L. Pughe-Sanford[†], W. Toler,
R. O. Grigoriev and M. F. Schatz

Center for Nonlinear Science and School of Physics, Georgia Institute of Technology, 837 State Street, Atlanta, GA 30332, USA

CJC, 0000-0002-3637-7841; JLP-S, 0000-0002-0208-2439;
WT, 0000-0003-1770-7996; ROG, 0000-0001-6220-4701;
MFS, 0000-0003-2768-8688

Recent work shows that recurrent solutions of the equations governing fluid flow play an important role in structuring the dynamics of turbulence. Here, an improved version of an earlier method (Krygier *et al.* 2021 *J. Fluid. Mech.* **923**, A7 and Crowley *et al.* 2022 *Proc. Natl Acad. Sci. USA* **119**, e2120665119) is used for detecting and analyzing intervals of time when turbulence 'shadows' (spatially and temporally mimics) recurrent solutions in both numerical simulations and laboratory experiments. We find that all the recurrent solutions shadowed in numerics are also shadowed in experiment, and the corresponding statistics of shadowing agree. Our results set the stage for experimentally grounded dynamical descriptions of turbulence in a variety of wall-bounded shear flows, enabling applications to forecasting and control.

This article is part of the theme issue 'Taylor–Couette and related flows on the centennial of Taylor's seminal *Philosophical Transactions* paper (part 1)'.

1. Introduction

At the start of his 1923 tour de force [1], Taylor stated, 'A great many attempts have been made to discover some mathematical representation of fluid instability, but so far they have been unsuccessful in every case'. Taylor illustrated, for the first time, how appropriate solutions to the equations governing fluid motion can be harnessed to make predictions about

---

[†] Joint first authors.

THE ROYAL SOCIETY
PUBLISHING

unstable behaviours that may be tested quantitatively in experiments. Specifically, in the case of flow between concentric, independently rotating cylinders (Taylor–Couette flow (TCF)), Taylor demonstrated how unstable solutions to the governing equations, linearized about a base state (Couette flow), can signal the transition to a new stable, non-turbulent flow (e.g. Taylor–Vortex flow); the remarkable quantitative agreement between predictions and observations that Taylor found established linear stability analysis as a core methodology for the prediction of flow transitions in TCF, Rayleigh–Bénard convection and numerous other problems in fluid mechanics [2]. Following in Taylor's footsteps, we study the same system (TCF) and also show how knowledge of unstable solutions can be exploited to make experimentally testable predictions; however, in the present work, behaviours of unstable solutions themselves, in their full nonlinear glory, are of primary interest, rather than those of linearized versions, which serve chiefly as indicators of shifts between stable nonlinear states.

Hopf conjectured that dissipation confines the dynamics of fluid motion to a low-dimensional subset of the state space, i.e. the inertial manifold [3]. He was also credited by Kraichnan as conceptualizing turbulence as a meandering walk between fleeting flow patterns [4, section A1.5]. Long-established observations [5] of these patterns (coherent structures) have suggested their relation to unstable solutions. Moore and Speigel were the first to advocate a description of turbulence in terms of unstable periodic solutions [6,7]. Christiansen *et al.* [8] were the first to apply this description to a spatially extended system in the context of the Kuramoto–Sivashinsky equation.

The advent of advanced numerical methods such as Newton–Krylov solvers [9] has enabled the computation of unstable, recurrent solutions, which can exhibit spatial [10] and temporal [11] features qualitatively similar to those of coherent structures observed in the laboratory. Consequently, such unstable solutions have become known as exact coherent structures (ECSs). These numerical results provide additional compelling evidence that ECSs play a key role in guiding fluid turbulence. For more history on the development of a dynamical framework for turbulence, we point the reader to refs. [12] and [4, section A1.5].

Building on a recent experimental study of a transitional quasi-two-dimensional flow [13], we show that ECSs play important and persistent roles in guiding the time evolution of three-dimensional, experimentally observable turbulence. The simplest types of ECSs that occur in turbulence are equilibria [14–18] and, in systems possessing a continuous spatial symmetry (e.g. circular symmetry in TCF), traveling waves [15,19–26], which are equilibria in suitable co-moving reference frames. Unstable periodic orbits [11,27] represent more complicated ECSs; they have been found to characterize turbulent behaviours in quasi-two-dimensional flow experiments [13]. In systems with a continuous symmetry, such as the pipe flow, snapshots of turbulence in numerical simulations [28,29] are found to resemble unstable relative periodic orbits (RPOs), which are time periodic in a co-moving reference frame.

The TCF geometry is ideally and uniquely suited for testing the ECS framework in the context of three-dimensional wall-bounded flows due to a natural periodicity in the streamwise (azimuthal) direction, which enables the boundary conditions of numerics and experiments to be matched, thereby facilitating direct comparison of computed ECSs with laboratory observations. Numerical simulations, in a different TCF configuration, previously demonstrated that turbulent TCF frequently and repeatedly shadows—i.e. emulates the spatial *and* temporal structure of—both RPOs and traveling waves [30]. Shadowing was later observed experimentally in the TCF configuration used here [31]. This article presents a comprehensive analysis of shadowing in numerical and experimental setups that are directly comparable. Both the experimental and numerical turbulence is found to shadow every RPO considered. Moreover, the frequency with which different RPOs are shadowed in experiment agrees well with the frequency of shadowing in the numerics.

This article is organized as follows: the particulars of TCF in this study are outlined in §2, and key aspects of the ECSs identified and explored herein are described in §3. The phenomenon of shadowing is described from a state-space perspective in §4, and the procedures for detecting

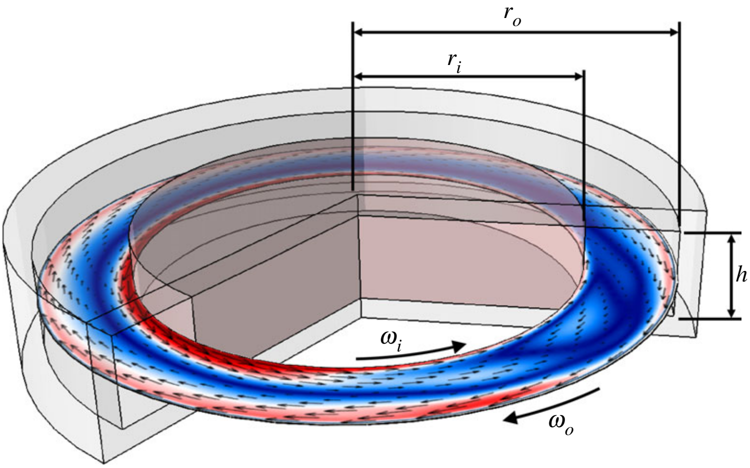

Figure 1. Turbulence is visualized in a laboratory flow between concentric, independently rotating cylinders with radii r_i and r_o and corresponding angular velocities ω_i and ω_o. Fluid is confined between the cylinders and bounded axially by end caps co-rotating with the outer cylinder. The azimuthal velocity, u_θ, is plotted in the horizontal cross-section, $z \approx h/2$, of the flow volume as a black vector field. The colourmap indicates the magnitude of deviations from the azimuthal mean flow, $\|u_\theta - \langle u_\theta \rangle\|$, where red (blue) is large (small). (Online version in colour.)

shadowing in turbulence experiments are discussed in §5. Results are presented in §6, and conclusions are presented in §7.

2. Experimental system

The geometry of the TCF apparatus used in this study, illustrated in figure 1, is characterized by two geometric parameters: the radius ratio $\eta = r_i/r_o$ and the aspect ratio $\Gamma = h/(r_o - r_i)$, where $r_i = 50$ mm and $r_o = 70.24$ mm are, respectively, the inner and outer radii of the flow domain. In his seminal paper, Taylor explored the $\Gamma \gg 1$ limit in which boundary effects of the top and bottom end caps are negligible; in contrast, we investigate the small aspect ratio ($\Gamma = 1$) and medium gap ($\eta = 0.71$) parameter regime, in which the end effects play a substantial role in driving the fluid motion. Relevant prior studies for this geometry are summarized in [30].

The inner and outer cylindrical walls of the Taylor–Couette apparatus rotate with angular velocities ω_i and ω_o, respectively, with the top and bottom endcaps co-rotating with the outer wall. Thus, two Reynolds numbers

$$\mathrm{Re}_i = \frac{r_i \omega_i (r_o - r_i)}{\nu} \quad \text{and} \quad \mathrm{Re}_o = \frac{r_o \omega_o (r_o - r_i)}{\nu},$$

can be used to characterize the external driving of the fluid. Here, ν is the kinematic viscosity. We investigate the case of counter-rotating boundaries $\mathrm{Re}_o = -200$ and $\mathrm{Re}_i = 500$.

The experimental TCF apparatus was constructed to be fully transparent to allow for optical access and, therefore, velocimetry measurements anywhere in the flow domain. Time-resolved azimuthal and radial velocity measurements near the horizontal midplane were sufficient in characterizing the dynamics despite the flow having nontrivial structure in the axial direction [31]. Here, the experimental setup and velocimetry techniques are identical to that of [31]; velocity is measured in a horizontal cross-section, as depicted in figure 1.

Table 1. Properties of known RPOs in our TCF system at $\mathrm{Re}_i = 500$ and $\mathrm{Re}_o = -200$. The table lists the temporal period, T; azimuthal shift, Φ; dimension of the unstable manifold of each solution, N^u; and escape time, γ^{-1}. Both T and γ^{-1} are reported in non-dimensional units, normalized by the viscous time scale $(r_o - r_i)^2/\nu \approx 271$ s. The number of unstable directions associated with each RPO is $N^u - 2$.

	T	Φ	N^u	γ^{-1}
RPO_1	0.196	1.043	9	0.0246
RPO_2	0.177	0.856	7	0.0209
RPO_3	0.234	0.448	9	0.0260
RPO_4	0.200	0.199	8	0.0299
RPO_5	0.422	0.443	7	0.0336
RPO_6	0.419	0.425	8	0.0358
RPO_7	0.164	0.481	8	0.0342
RPO_8	0.215	5.799	8	0.0464

3. Exact coherent structures in TCF

The presence of a continuous (rotational) symmetry in Taylor–Couette flow implies that the most common ECSs will be relative, e.g. traveling waves or RPOs [28,30,32]. RPOs are solutions satisfying

$$\mathbf{u}(r,\theta,z,t) = \mathbf{u}(r,\theta+\Phi,z,t+T), \tag{3.1}$$

for some temporal period T and rotation angle Φ. RPOs are time-periodic solutions in a co-moving reference frame of angular speed Φ/T.

The numerical turbulent trajectory and recurrent solutions analyzed here are taken from [31], providing us with a library of eight recurrent solutions, $(\mathbf{u}_n, T_n, \Phi_n)_{n=1}^{8}$, that satisfy both the Navier–Stokes equation and equation (3.1) to numerical precision. Their period, azimuthal shift, and stability are summarized in table 1. Details about the numerical code and resolution may be found in [31].

Additional ECSs can be found by numerical continuation of the eight original RPOs in any of the parameters (Re_i, Re_o, Γ, and η) [33]. For instance, continuation in Re_i yields solution branches that commonly turn around at saddle-node bifurcations, returning to the original value of Re_i. This procedure either connects the original RPOs (e.g. RPO_5 and RPO_6 as shown in figure 2) or defines new ones. Note that, aside from rare exceptions, the properties of the RPOs are not particularly sensitive to the choice of parameters. This enables comparison to experiment that has an uncertainty associated with how parameters (mainly Re_i and Re_o) are set or measured.

In the presence of continuous symmetry, existence of an ECS implies the existence of a continuum of symmetry-related copies of that ECS (e.g. the corresponding group orbit). In particular, for an RPO described by the velocity field $\mathbf{u}_n(r,\theta,z,t)$, the symmetry-related copies $\mathbf{u}_n(r,\theta+\phi,z,t+\tau)$ also satisfy both the governing equations and the condition (3.1) for any τ and ϕ, which are most naturally thought of as the group parameters describing translational symmetry in time and angular orientation, respectively. Of course, not all symmetry-related solutions are necessarily distinct, e.g. $\tau = kT_n$ and $\phi = k\Phi_n$ with any integer k yield identical flows related by a shift in the temporal origin.

Consider the flow with an initial condition $\mathbf{u}_n(r,\theta,z,0)$. In the typical case when Φ_n is an irrational multiple of 2π, this flow is quasi-periodic in the laboratory frame and is characterized by two frequencies, $\Omega_1 = 2\pi/T$ and $\Omega_2 = \Phi_n/T_n$. The condition (3.1) ensures that this flow can be represented by properly rotated copies of the RPO $\mathbf{u}_n(r,\theta,z,\tau)$ with $0 \le \tau < T_n$, so we only need to compute one period to represent the flow at all times. Topologically, a quasi-periodic flow corresponds to a torus in state space which, for the case of an RPO, can be fully parameterized

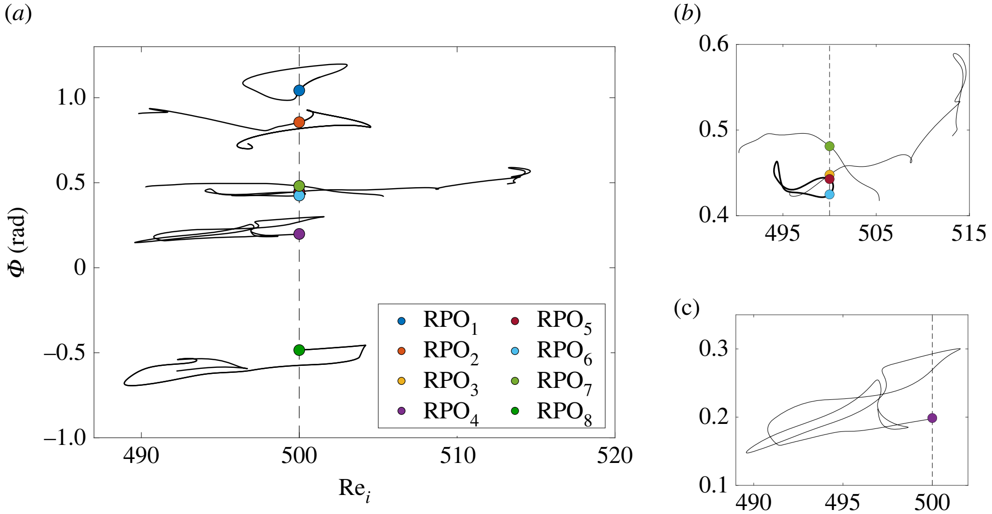

Figure 2. (*a*) Numerically obtained solution branches associated with RPOs listed in table 1 obtained by continuation in Re_i. The RPOs analyzed in this article are shown as coloured points. For each branch, the azimuthal shift $\varPhi$ is plotted as a function of Re_i, with the initial solution at $\mathrm{Re}_i = 500$ plotted as a solid marker. (*b*,*c*) Regions where RPOs have overlapping branch structure are enlarged. Note that RPO_5 and RPO_6 lie on the same continuation curve, which is bolded in (*b*) for clarity; they are born from a bifurcation at $\mathrm{Re}_i = 500.39$. (Online version in colour.)

by the velocity field $\mathbf{u}_n(r, \theta + \phi, z, t + \tau)$ with $\tau \in [0, T_n)$ and $\phi \in [0, 2\pi)$. As a result, for any $\varPhi_n$ which is an irrational multiple of 2π, the set of all distinct translations span the surface of a torus, and all points on this torus may be parametrized by the cyclic temporal coordinate τ and angular coordinate ϕ. On the surface of this torus, temporal evolution is fundamentally simple in the (τ, ϕ) parameterization:

$$\left.\begin{aligned}\tau &= t + \tau_0 - kT_n\\ \text{and}\qquad \phi &= \phi_0 + k\varPhi_n\end{aligned}\right\}\tag{3.2}$$

for $t \in [kT_n, (k+1)T_n)$. This parameterization of the torus is analogous to the one used to parameterize periodic orbits [13] and unstable manifolds [18].

4. State-space geometry and shadowing

For an observer, an evolving fluid flow is most naturally described by a time-dependent velocity field. Geometrically, the same flow can be described by a one-dimensional trajectory in a high-dimensional state space. State space can be constructed from the full velocity field with any smooth, invertible mapping, such as a Fourier or proper orthogonal decomposition. Regardless of the choice of mapping, at every instant in time, the entire flow field corresponds to a single point in the state space. As time evolves, this point traces out a curve which, for a turbulent flow, has a very complicated and highly tangled shape.

These tangled trajectories are direct analogues of chaotic solutions to systems of nonlinear differential equations such as the well-known Lorenz [34] or Rössler [35] systems. As a result of dissipation, chaotic trajectories are attracted, and eventually confined to a lower-dimensional manifold known as the chaotic attractor [3]. In addition to chaotic trajectories, the attractor also contains an infinite number of unstable recurrent solutions, such as periodic orbits. Quite analogously, the trajectory describing a turbulent flow is also confined to a relatively low-dimensional manifold, which contains unstable recurrent solutions (ECSs) of the Navier–Stokes equations. Just as in the low-dimensional setting, ECSs represent low-dimensional invariant sets: e.g. equilibria correspond to points (zero-dimensional sets), traveling waves and time-periodic

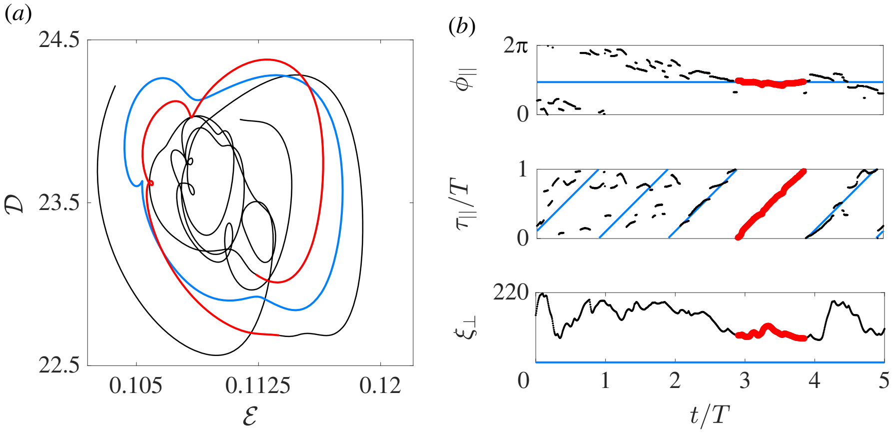

Figure 3. An example of shadowing, from numerical simulation, using different projections of state space. (*a*) A traditional projection onto the two-dimensional subspace spanned by the energy density $\mathcal{E}$ and dissipation rate $\mathcal{D}$ of the non-dimensional velocity fields. (*b*) The same interval of time, projected onto the local coordinates: azimuthal phase $\phi_{||}$, temporal phase $\tau_{||}$ and non-dimensional distance $\xi_{\perp}$. In *a*, *b*, RPO_1 is shown in blue and turbulent flow is shown in black (red) outside (inside) the shadowing interval. The interval shown corresponds to the shadowing event at $t \approx 17$ min in figure 7. (Online version in colour.)

solutions correspond to loops (one-dimensional sets), and quasi-periodic solutions such as RPOs correspond to tori (two-dimensional sets).

A geometrical representation of turbulence is particularly helpful for both understanding and quantifying the relation between turbulence and recurrent solutions. Dynamical similarity between any two evolving flows is described by the shape and proximity of the corresponding trajectories in state space. Points that are close in state space, as characterized by Euclidean distance $||\mathbf{u}-\mathbf{v}||$, correspond to flows $\mathbf{u}$ and $\mathbf{v}$ with similar velocity fields, where

$$||\mathbf{u}|| = \left[\iint_S (\mathbf{u}\cdot\mathbf{u})\,\mathrm{d}S\right]^{1/2}. \tag{4.1}$$

Here, S corresponds to a horizontal slice, $S=[0,2\pi)\times[r_i,r_o]$, at the midplane in numerics and 1.5 mm above the midplane in experiment. Similarity in the shape of (portions of) a pair of trajectories in the state space implies qualitative similarity in the evolution of the corresponding flows. Quantitative similarity additionally requires that the state-space speed be similar for the two trajectories [13].

While comparison of a pair of flow snapshots is straightforward, quantifying the similarity of evolving flows is far less trivial. Generic low-dimensional projections frequently used in the literature can be misleading. Consider, for instance, the projection onto the subspace spanned by two common global observables, the energy density

$$\mathcal{E} = \frac{1}{\mathrm{Re}^2 S}||\mathbf{u}^2|| \tag{4.2}$$

and the rate of energy dissipation

$$\mathcal{D} = \frac{1}{\mathrm{Re}^2 S}||(\nabla\times\mathbf{u})^2||, \tag{4.3}$$

normalized here by the characteristic velocity scale $\mathrm{Re} = |\mathrm{Re}_i - \mathrm{Re}_o|/2$. As shown in figure 3*a*, this projection suggests that a portion of turbulent trajectory (shown in red) has a shape qualitatively similar to that describing RPO_1 (shown in blue). The corresponding turbulent flow might indeed be similar to this RPO with a very particular orientation. However, the exact same projection would also describe an RPO with a completely different orientation that is not at all similar to the turbulent flow (i.e. lies far from it in the full state space).

A more appropriate choice of coordinates is local rather than global and is informed by the symmetries of the problem. In the neighbourhood of an RPO, every trajectory $\mathbf{u}(t)$ can be well parameterized [30] using the distance transverse to the torus

$$\xi_\perp(t) = \min_{\tau,\phi} \xi_n(t,\tau,\phi)$$

and the two phases along its surface,

$$\{\tau_{||}(t), \phi_{||}(t)\} = \arg\min_{\tau,\phi} \xi_n(t,\tau,\phi)$$

defined relative to the RPO, where

$$\xi_n(t,\tau,\phi) = ||\mathbf{u}(r,\theta,z,t) - \mathbf{u}_n(r,\theta+\phi,z,\tau)||. \tag{4.4}$$

We will drop the subscript n when it is clear which solution is being considered.

For a trajectory lying on the torus representing the RPO, $\xi_\perp(t)=0$, and its evolution is described by equation (3.2) exactly. For $\xi_\perp(t)$-small, one would expect equation (3.2) to be satisfied approximately. Indeed, this is what we find for the segment of the turbulent flow shown in red in figure 3. As figure 3*b* illustrates, over an interval comparable to one period of RPO$_1$, the temporal phase $\tau_{||}(t)$ indeed faithfully follows a diagonal, straight line, indicating that turbulent flow evolves at the same rate as the RPO. The azimuthal phase $\phi_{||}(t)$ remains nearly constant over the same interval.

5. Detecting shadowing in experiment

Computation of the phases corresponding to the minima of the distance $\xi(t,\tau,\phi)$ becomes unreliable in experiment due to unavoidable noise. To address this, we instead quantify dynamical similarity by time averaging the distance over a finite time interval $t\in[t_0-I/2, t_0+I/2]$:

$$\bar{\xi}(t_0,\tau_0,\phi_0) = \frac{1}{I}\int_{t_0-I/2}^{t_0+I/2} \xi(t,\tau(t),\phi(t))\,\mathrm{d}t, \tag{5.1}$$

where the two phases are assumed to satisfy equation (3.2) at all times. Shadowing of the respective RPO over this interval is expected for $\bar{\xi}$ sufficiently small and, indeed, this is what we find, as illustrated in figure 4.

The natural time scale associated with a close pass to an RPO is given by the inverse of the escape rate defined by [36]:

$$\gamma_n = \sum_i \mathrm{Re}(\lambda_{n,i}),$$

where $\lambda_{n,i}$ are the unstable Floquet exponents of RPO$_n$. Hence, we take $I=\gamma_n^{-1}$ for detecting shadowing of the corresponding RPO. As table 1 shows, these escape times tend to be quite short compared to the periods of the respective RPOs. The shadowing event discussed in the previous section is particularly long: its duration is comparable to one entire period of the RPO (almost $10I$).

To characterize $\bar{\xi}$ as 'small' or 'large', a distance scale is needed. Generically, a characteristic distance scale, L, can vary substantially throughout state space, as the density of trajectories in state space itself varies. This characteristic distance can even vary along a single recurrent solution. As a result, intervals of shadowing that occur in regions where L is large will result in a larger value of $\bar{\xi}$ compared with shadowing events of similar quality in regions where L is small. Thus, to compensate for this intrinsic variation in distance L within state space, we define a normalized average distance

$$d_n(t_0,\tau_0,\phi_0) = \frac{1}{I}\int_{t_0-I/2}^{t_0+I/2} \frac{\xi_n(t,\tau(t),\phi(t))}{L(\tau(t),\phi(t))}\,\mathrm{d}t, \tag{5.2}$$

where $L(\tau,\theta)$ is the characteristic distance scale of state space in the vicinity of the RPO, $\mathbf{u}(\tau,\theta)$. In general, L may depend on θ, e.g. due to experimental bias. In TCF, rotational symmetry implies

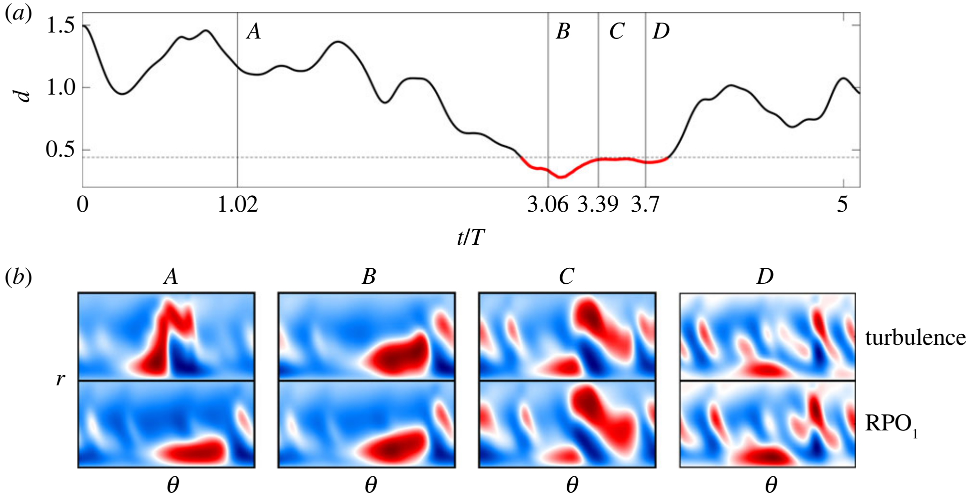

Figure 4. Comparison of the flow fields representing turbulent flow and relative periodic orbit (RPO$_1$) during the same interval of numerical simulation illustrated in figure 3. (*a*) The distance d to the RPO with the shadowing portion is shown in red. A dashed horizontal line is placed at $d = 0.44$. (*b*) The flow fields corresponding to the time instances are labelled with vertical lines in *a*. Here and later, the mean-subtracted azimuthal velocity, $u_\theta - \langle u_\theta \rangle_t$, is plotted for turbulent flow and the corresponding RPO, where red (blue) is positive (negative). Each rectangular box represents the annular region spanned by r and θ, where r_i is on (*a*) and r_o is on (*b*). In figure 7*a*, this event corresponds to the minimum at $t \approx 17$ min. (Online version in colour.)

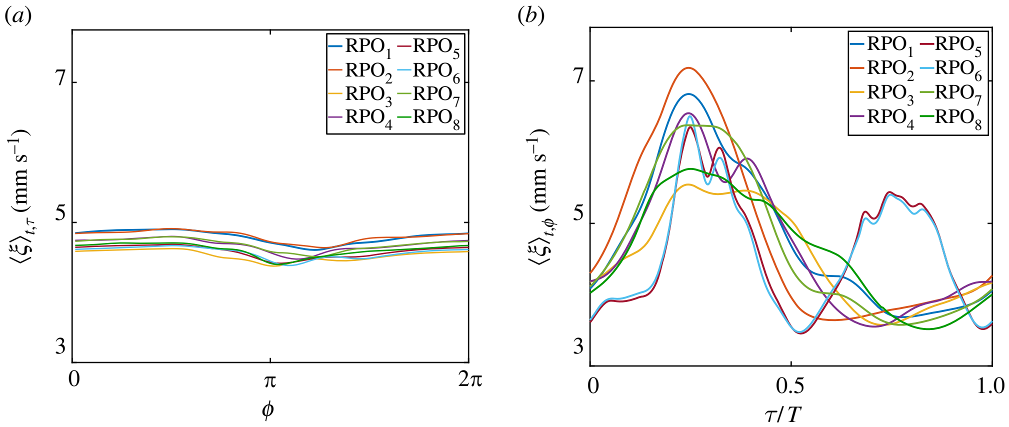

Figure 5. Phase dependence of the experimentally observed distance defined in equation (4.4) averaged (*a*) over t and τ and (*b*) over t and ϕ. Here, $\langle \cdot \rangle_x$ denotes an average over x. (Online version in colour.)

that L should be independent of θ, and this is what we find (see figure 5*a*). On the other hand, the dependence on τ is quite pronounced for all RPOs, as figure 5*b* illustrates. Thus, we define the characteristic distance scale,

$$L(\tau) = \left[\frac{1}{2\pi T} \int_0^{2\pi} \mathrm{d}\theta \int_0^T \frac{1}{\xi(t,\tau,\theta)}\, \mathrm{d}t \right]^{-1}, \tag{5.3}$$

as the harmonic mean distance between turbulent flow and a given RPO, where T is the duration of the turbulent trajectory. A harmonic mean weighs small distances more than would an arithmetic mean, which provides a more local measure of the characteristic distance to the RPO.

The normalized distance d provides a more uniform measure of the quality of shadowing. Low values correspond to intervals when both the turbulent flow field and its time evolution are well captured by the specific recurrent solution. For larger values of d, the apparent similarity of the two flow fields and dynamics is less striking. The degree of similarity between the two flows that define shadowing is, however, subjective. As figure 4 illustrates, in numerical simulation, $d = 0.44$ gives a threshold of visual similarity between the flow fields. In contrast, experimental noise increases ξ, yielding a higher threshold value.

6. Results

In a dynamical systems framework, turbulence is described by a sequence of visits to the neighbourhoods of different recurrent solutions. In support of this picture, we find that, in both numerics and experiment, turbulence shadows our library of recurrent solutions sequentially and that every known solution is shadowed. Representative shadowing events in experiment are presented in figure 6 for the distinct RPOs 1–5, 7 and 8.

Despite the relatively small library of RPOs, shadowing is observed quite often, as demonstrated in figure 7. Similar to what was found in the geometry examined by [30], we find that a semi-quantitative dynamical description of turbulence may require only $\mathcal{O}(10)$ recurrent solutions when shadowing events of the quality shown in figure 4 are of interest. Of course, the accuracy of this dynamical description is directly related to the choice of the shadowing threshold. With the threshold analyzed here, the RPO library provides a relatively coarse partitioning of the state space into the respective neighbourhoods. A finer partition corresponding to a lower threshold of d will require computing a larger library of recurrent solutions (not necessarily all RPOs).

The cumulative probability $P(d)$, which defines the likelihood that $d_n(t) < d$ over all RPOs and over all times, is plotted in figure 8*a*. The 33rd percentile is found to correspond to $d_0 = 0.44$ for the numerical dataset, and on average, $d_0 = 0.57$ for the two experimental datasets. As demonstrated in figure 4, events in this percentile show striking visual similarity between turbulence and the recurrent solutions. We consider the relative frequency,

$$f_n = \frac{P_n(d_0)}{\sum_i P_i(d_0)}, \tag{6.1}$$

with which each solution is shadowed in the 33rd percentile. Here, $P_n(d_0)$ is the probability that the distance d_n is below d_0. We find the distribution of f_n to be comparable between numerical turbulence and both experimental datasets, as illustrated in figure 8*b*, suggesting that statistical contribution of different recurrent solutions in experiment and numerical simulations is the same.

As first observed in [30], here we again find that turbulence often shadows more than one solution at once. Hence, turbulence may be described by multiple solutions simultaneously, as illustrated in figure 7 and evidenced in figure 9. This observation is rather surprising, given the small size of the RPO library. One might expect turbulence to shadow multiple solutions if these solutions are born from a nearby bifurcation in parameter space and, consequently, are themselves almost indistinguishable. This is the case for RPO_5 and RPO_6 in our study, which are related via a saddle-node bifurcation (see figure 2). These two solutions are almost always shadowed simultaneously, which is unsurprising given their proximity in state space, as shown in figure 10*a*.

However, it is also possible for turbulence to simultaneously shadow RPOs that are not related through a nearby bifurcation, as long as portions of these RPOs lie close in state space. Figure 9 illustrates an example of this simultaneous shadowing in physical space; both RPO_3 and RPO_8 describe the spatial structure of turbulent flow and its evolution over an interval of 30 s. In this interval, turbulence is similar to both RPO_3 and RPO_8 in the state space, as illustrated in figure 10*b*. In fact, RPO_3 and RPO_8 effectively shadow each other during this interval as well.

While it is well known that longer orbits shadow shorter ones in low-dimensional chaotic systems, the results presented here suggest that RPOs with comparable periods can have segments that lie close enough in state space to be shadowed simultaneously. Similarly, [30] found

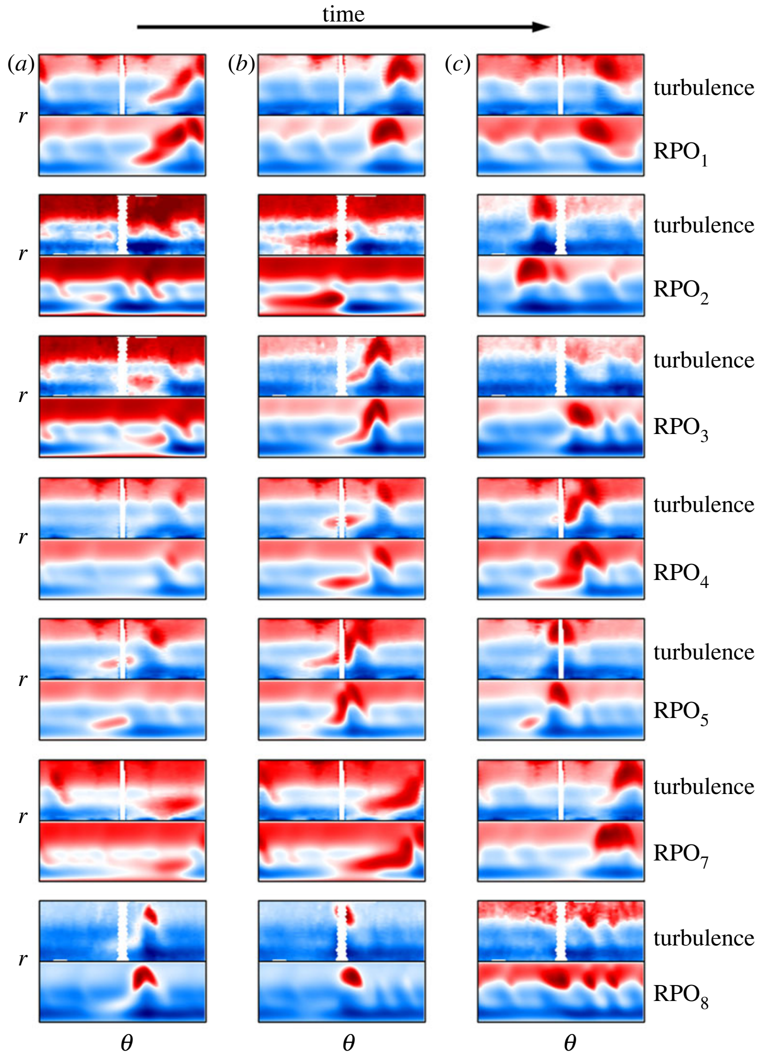

Figure 6. Experimental observations of turbulence shadowing each of the known recurrent solutions (due to the similarity of RPO$_5$ and RPO$_6$, only RPO$_5$ is shown). The vertical band represents experimental data missing because of non-uniform illumination. In each example, time advances from (*a*) to (*c*), where the separation between each column is approximately 6.4 s, or about one-eighth of the typical period. No two events shown here are simultaneous. (Online version in colour.)

turbulence to simultaneously shadow segments of an RPO along with a travelling wave. This suggests that turbulence generically shadows segments of possibly more than one ECS, rather than a unique ECS for its entire length [13,30,37]. This is especially true for longer orbits.

7. Conclusion

This study presents a comprehensive experimental test of the conjecture that turbulence can be viewed as a deterministic walk between neighbourhoods of distinct unstable solutions of the governing equations. In small-aspect-ratio counter-rotating Taylor–Couette flow, a number of such solutions have been found previously; they all correspond to RPOs [31]. We firmly establish that turbulence shadows every one of these RPOs, fleetingly but repeatedly spending a substantial fraction of time in their neighbourhoods. Moreover, we find that the frequency with which each solution is shadowed in experiment agrees with numerical predictions. We find that turbulence

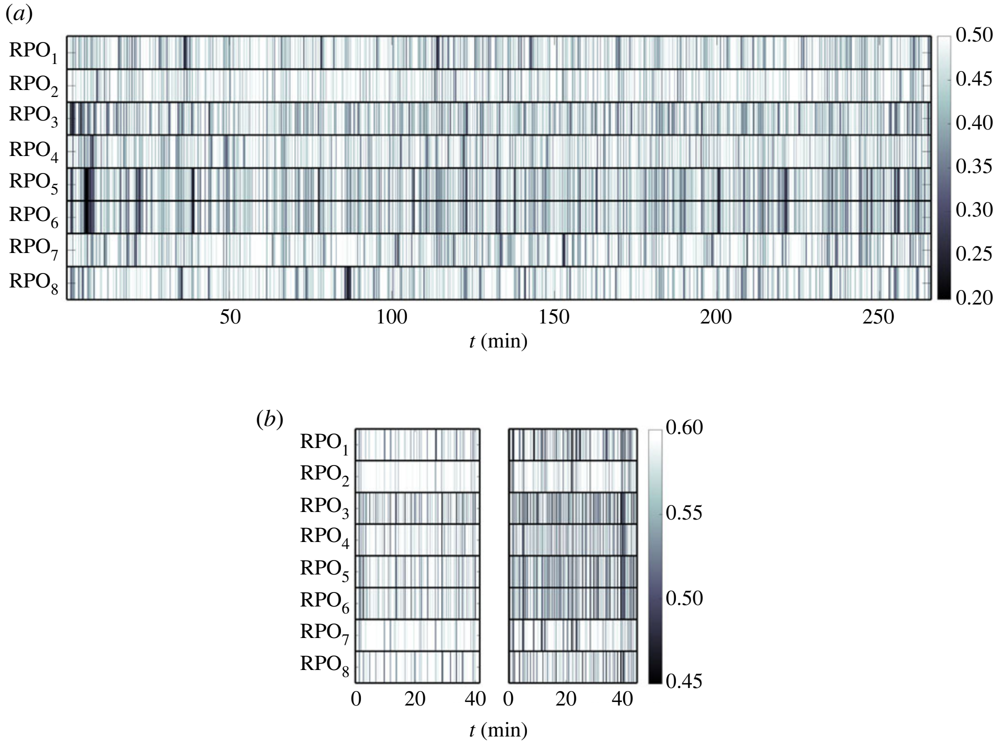

Figure 7. Turbulence frequently shadows RPOs in (*a*) numerical simulation and (*b*) experiment. For each RPO, *d* is plotted as a function of time using a colour gradient; darker vertical lines indicate shadowing events—time intervals during which RPOs are being tracked by turbulence. Darker intervals correspond to higher quality shadowing events. Two separate runs are shown in experiment, of roughly equal length. A slight difference in noise floor is notable between datasets. (Online version in colour.)

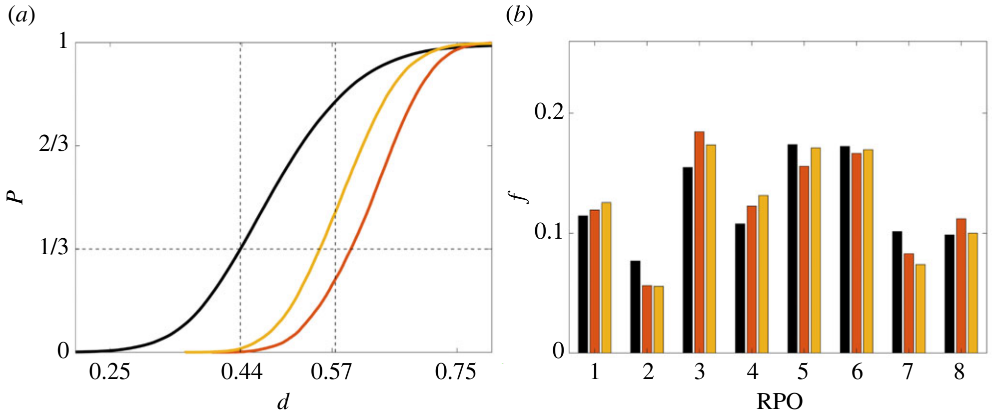

Figure 8. (*a*) Cumulative probability of *d* for the numerical dataset (black), and the two experimental datasets (red and yellow, respectively). A horizontal dashed line denotes the 33rd percentile, and vertical dashed lines represent the corresponding distance threshold for numerics and experiment. (*b*) The shadowing frequency f_n is plotted for each of the eight RPOs. The same colour palette as shown in (*a*) is used to denote the three datasets. (Online version in colour.)

tends to shadow RPOs for a fraction of the period and that, when it does so, turbulence often shadows multiple ECSs at once. Given that turbulence never approaches any solution particularly closely, it is surprising how well and how often these solutions predict the evolution of turbulent flow.

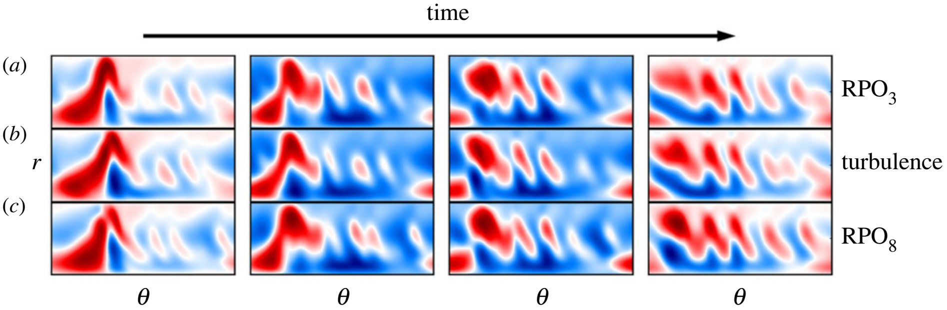

Figure 9. Example from numerical simulation of turbulence (*b*) shadowing both RPOs 3 (*a*) and 8 (*c*) for $t \in (15\,\text{s}, 40\,\text{s})$. (*a–c*) evolve in time from left to right. The inner three rows display shadowing between all three solutions. Notice that, when turbulence shadows multiple solutions, it resembles all solutions it shadows. During such intervals, the recurrent solutions may also be considered to shadow each other. (Online version in colour.)

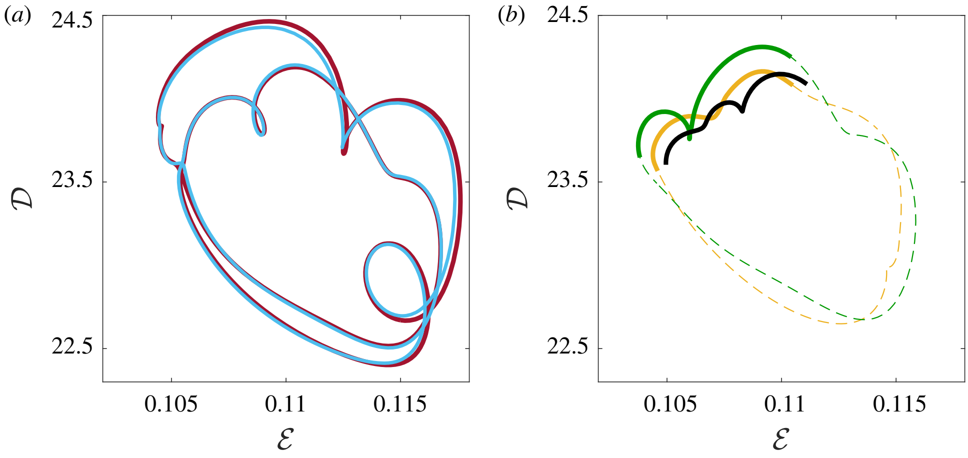

Figure 10. Low-dimensional projections of (*a*) RPO$_5$ (deep red) and RPO$_6$ (light blue) and (*b*) RPO$_3$ (yellow) and RPO$_8$ (green) in the state space. Volumetric kinetic energy and dissipation of the velocity field are used as coordinates. (*b*) The intervals of each RPO that are displayed in figure 9 are bolded, and a segment of numerical turbulence shadowing these segments is overlaid in black. (Online version in colour.)

With the sparse library of ECS used here, we are only able to capture a semi-quantitative description of turbulence. For instance, in the example shown in figure 3*a*, both the energy and dissipation rate are found to differ rather substantially from those characterized by RPO$_1$ despite the flow fields appearing almost indistinguishable. However, as more ECS are considered, turbulence will make closer visits to individual solutions, and the accuracy with which observables are predicted during shadowing will increase. Interestingly, it is possible to predict turbulent averages fairly accurately using a relatively small collection of shadowed orbits [37].

The shadowing analysis opens new doors for describing turbulence in terms of a variety of invariant sets. The approach used here can be extended for detecting shadowing of other types of recurrent flows as well as non-recurrent flows. In particular, turbulence has been observed [17,18] to shadow unstable manifolds as well. Heteroclinic connections [38,39], which are the intersection of a stable manifold of one solution and an unstable manifold of another solution and describe the dynamical transition between the two solutions, are likely shadowed as well.

Detecting heteroclinic shadowing events could strengthen the predictive power of Hopf's picture. Heteroclinic connections define the possible sequences of ECS that turbulence can shadow. Heteroclinic connections could also play an important role in describing extreme events, which are not recurrent and unlikely to be described by ECS.

ECS have already generated much insight into fluid turbulence. For instance, ECS capture self-sustaining processes that maintain wall-bounded turbulence [40]) and elucidate the transition to turbulence [41,42]. This study provides corroborating experimental and numerical validations that ECSs describe the spatiotemporal structure of sustained turbulence; basically, ECS serve as a backbone for turbulence [43]. The ability to detect shadowing is also crucial for implementing reduced descriptions of turbulence, such as symbolic dynamics [37]. Invariant sets such as equilibria, periodic orbits and heteroclinic connections collectively define a road map of turbulence. Further development of a dynamical framework based on invariant sets [30,31,37,38] could eventually enable forecasting and control of turbulence.

Data accessibility. The data and codes for this paper can be accessed at the following github repository: https://github.com/cdggt/tcf/tree/main/eta0.71.

Authors' contributions. C.J.C.: conceptualization, data curation, formal analysis, investigation, methodology, software, validation, visualization, writing—original draft and writing—review and editing; J.L.P.-S.: conceptualization, data curation, formal analysis, investigation, methodology, software, validation, visualization, writing—original draft and writing—review and editing; W.T.: conceptualization, data curation, formal analysis, investigation, methodology, software, validation, visualization, writing—original draft and writing—review and editing; R.O.G.: conceptualization, funding acquisition, investigation, methodology, project administration, supervision, writing—original draft and writing—review and editing; M.F.S.: conceptualization, funding acquisition, investigation, methodology, project administration, supervision, writing—original draft and writing—review and editing.

All authors gave final approval for publication and agreed to be held accountable for the work performed therein.

Conflict of interest declaration. We declare we have no competing interests.

Funding. We gratefully acknowledge financial support by ARO (Grant nos. W911NF-15-1-0471 and W911NF-16-10281) and by NSF (Grant no. CMMI-1725587).

Acknowledgements. Numerical simulations used the Taylor–Couette flow code written by Marc Avila. Michael C. Krygier developed numerical tools for finding and continuing recurrent solutions.

References

1. Taylor GI. 1923 Stability of a viscous liquid contained between two rotating cylinders. *Phil. Trans. R. Soc. Lond. A* **223**, 289–343. (doi:10.1098/rsta.1923.0008)
2. Cross MC, Hohenberg PC. 1993 Pattern formation outside of equilibrium. *Rev. Mod. Phys.* **65**, 851–1112. (doi:10.1103/RevModPhys.65.851)
3. Hopf E. 1948 A mathematical example displaying features of turbulence. *Commun. Pure Appl. Math.* **1**, 303–322. (doi:10.1002/(ISSN)1097-0312)
4. Cvitanović P, Artuso R, Mainieri R, Tanner G, Vattay G. 2016 *Chaos: classical and quantum*. Copenhagen: Niels Bohr Institute.
5. Hussain AF. 1983 Coherent structures—reality and myth. *Phys. Fluids* **26**, 2816–2850. (doi:10.1063/1.864048)
6. Moore DW, Spiegel EA. 1966 A thermally excited non-linear oscillator. *Astrophys. J.* **143**, 871. (doi:10.1086/148562)
7. Spiegel EA. 1987 Chaos: a mixed metaphor for turbulence. *Proc. R. Soc. Lond. A* **413**, 87–95. (doi:10.1098/rspa.1987.0102)
8. Christiansen F, Cvitanovic P, Putkaradze V. 1997 Spatiotemporal chaos in terms of unstable recurrent patterns. *Nonlinearity* **10**, 55–70. (doi:10.1088/0951-7715/10/1/004)
9. Viswanath D. 2007 Recurrent motions within plane Couette turbulence. *J. Fluid Mech.* **580**, 339–358. (doi:10.1017/S0022112007005459)
10. Itano T, Generalis SC. 2009 Hairpin vortex solution in planar Couette flow: a tapestry of knotted vortices. *Phys. Rev. Lett.* **102**, 114501. (doi:10.1103/PhysRevLett.102.114501)

11. Cvitanović P, Gibson J. 2010 Geometry of the turbulence in wall-bounded shear flows: periodic orbits. *Phys. Scr.* **T142**, 014007. (doi:10.1088/0031-8949/2010/T142/014007)
12. Cvitanović P. 2013 Recurrent flows: the clockwork behind turbulence. *J. Fluid Mech.* **726**, 1–4. (doi:10.1017/jfm.2013.198)
13. Suri B, Kageorge L, Grigoriev RO, Schatz MF. 2020 Capturing turbulent dynamics and statistics in experiments with unstable periodic orbits. *Phys. Rev. Lett.* **125**, 064501. (doi:10.1103/PhysRevLett.125.064501)
14. Nagata M. 1990 Three-dimensional finite-amplitude solutions in plane Couette flow: bifurcation from infinity. *J. Fluid Mech.* **217**, 519–527. (doi:10.1017/S0022112090000829)
15. Clever RM, Busse FH. 1997 Tertiary and quaternary solutions for plane Couette flow. *J. Fluid Mech.* **344**, 137–153. (doi:10.1017/S0022112097005818)
16. Gibson JF, Halcrow J, Cvitanović P. 2008 Visualizing the geometry of state space in plane Couette flow. *J. Fluid Mech.* **611**, 107–130. (doi:10.1017/S002211200800267X)
17. Suri B, Tithof J, Grigoriev RO, Schatz MF. 2017 Forecasting fluid flows using the geometry of turbulence. *Phys. Rev. Lett.* **118**, 114501. (doi:10.1103/PhysRevLett.118.114501)
18. Suri B, Tithof J, Grigoriev RO, Schatz MF. 2018 Unstable equilibria and invariant manifolds in quasi-two-dimensional Kolmogorov-like flow. *Phys. Rev. E* **98**, 023105. (doi:10.1103/PhysRevE.98.023105)
19. Faisst H, Eckhardt B. 2003 Traveling waves in pipe flow. *Phys. Rev. Lett.* **91**, 224502. (doi:10.1103/PhysRevLett.91.224502)
20. Hof B, van Doorne CWH, Westerweel J, Nieuwstadt FTM, Faisst H, Eckhardt B, Wedin H, Kerswell RR, Waleffe F. 2004 Experimental observation of nonlinear traveling waves in turbulent pipe flow. *Science* **305**, 1594–1598. (doi:10.1126/science.1100393)
21. de Lozar A, Mellibovsky F, Avila M, Hof B. 2012 Edge state in pipe flow experiments. *Phys. Rev. Lett.* **108**, 214502. (doi:10.1103/PhysRevLett.108.214502)
22. Lemoult G, Gumowski K, Aider J-L, Wesfreid JE. 2014 Turbulent spots in channel flow: an experimental study. *Eur. Phys. J. E* **37**, 25. (doi:10.1140/epje/i2014-14025-2)
23. Park JS, Graham MD. 2015 Exact coherent states and connections to turbulent dynamics in minimal channel flow. *J. Fluid Mech.* **782**, 430–454. (doi:10.1017/jfm.2015.554)
24. Mellibovsky F, Meseguer A, Schneider TM, Eckhardt B. 2009 Transition in localized pipe flow turbulence. *Phys. Rev. Lett.* **103**, 054502. (doi:10.1103/PhysRevLett.103.054502)
25. Kerswell RR, Tutty OR. 2007 Recurrence of travelling waves in transitional pipe flow. *J. Fluid Mech.* **584**, 69–102. (doi:10.1017/S0022112007006301)
26. Eckhardt B, Zammert S. 2018 Small scale exact coherent structures at large Reynolds numbers in plane Couette flow. *Nonlinearity* **31**, R66–R77. (doi:10.1088/1361-6544/aa9462)
27. Kawahara G, Kida S. 2001 Periodic motion embedded in plane Couette turbulence: regeneration cycle and burst. *J. Fluid Mech.* **449**, 291–300. (doi:10.1017/S0022112001006243)
28. Budanur NB, Short KY, Farazmand M, Willis AP, Cvitanović P. 2017 Relative periodic orbits form the backbone of turbulent pipe flow. *J. Fluid Mech.* **833**, 274–301. (doi:10.1017/jfm.2017.699)
29. Willis AP, Cvitanović P, Avila M. 2013 Revealing the state space of turbulent pipe flow by symmetry reduction. *J. Fluid Mech.* **721**, 514–540. (doi:10.1017/jfm.2013.75)
30. Krygier MC, Pughe-Sanford JL, Grigoriev RO. 2021 Exact coherent structures and shadowing in turbulent Taylor-Couette flow. *J. Fluid Mech.* **923**, A7. (doi:10.1017/jfm.2021.522)
31. Crowley CJ, Pughe-Sanford JL, Toler W, Krygier MC, Grigoriev RO, Schatz MF. 2022 Turbulence tracks recurrent solutions. *Proc. Natl Acad. Sci. USA* **119**, e2120665119. (doi:10.1073/pnas.2120665119)
32. Meseguer A, Mellibovsky F, Avila M, Marques F. 2009 Families of subcritical spirals in highly counter-rotating Taylor-Couette flow. *Phys. Rev. E* **79**, 036309. (doi:10.1103/PhysRevE.79.036309)
33. Krygier MC. 2019 Exact coherent structures in turbulent small-aspect-ratio Taylor-Couette flow. Ph.D. thesis. GA: Georgia Institute of Technology.
34. Lorenz EN. 1963 Deterministic nonperiodic Flow. *J. Atmos. Sci.* **20**, 130–141. (doi:10.1175/1520-0469(1963)020<0130:DNF>2.0.CO;2)
35. Rössler OE. 1976 An equation for continuous chaos. *Phys. Lett. A* **57**, 397–398. (doi:10.1016/0375-9601(76)90101-8)
36. Kadanoff LP, Tang C. 1984 Escape from strange repellers. *Proc. Natl Acad. Sci. USA* **81**, 1276–1279. (doi:10.1073/pnas.81.4.1276)

37. Yalnız G, Hof B, Budanur NB. 2021 Coarse graining the state space of a turbulent flow using periodic orbits. *Phys. Rev. Lett.* **126**, 244502. (doi:10.1103/PhysRevLett.126.244502)
38. Suri B, Pallantla RK, Schatz MF, Grigoriev RO. 2019 Heteroclinic and homoclinic connections in a Kolmogorov-like flow. *Phys. Rev. E* **100**, 013112. (doi:10.1103/PhysRevE.100.013112)
39. Farano M, Cherubini S, Robinet J-C, De Palma P, Schneider T. 2019 Computing heteroclinic orbits using adjoint-based methods. *J. Fluid Mech.* **858**, R3. (doi:10.1017/jfm.2018.860)
40. Waleffe F. 1997 On a self-sustaining process in shear flows. *Phys. Fluids* **9**, 883–900. (doi:10.1063/1.869185)
41. Itano T, Toh S. 2001 The dynamics of bursting process in wall turbulence. *J. Phys. Soc. Jpn.* **70**, 703–716. (doi:10.1143/JPSJ.70.703)
42. Kreilos T, Eckhardt B. 2012 Periodic orbits near onset of chaos in plane Couette flow. *Chaos* **22**, 047505. (doi:10.1063/1.4757227)
43. Cvitanović P. 2013 Recurrent flows: the clockwork behind turbulence. *J. Fluid Mech.* **726**, 1–4. (doi:10.1017/jfm.2013.198)